

Die Grenzen der Chemie neu ausloten? It takes #HumanChemistry

Wir suchen kreative Chemikerinnen und Chemiker, die mit uns gemeinsam neue Wege gehen wollen – mit Fachwissen, Unternehmertum und Kreativität für innovative Lösungen. Informieren Sie sich unter:

evonik.de/karriere



www.aem-journal.com

In Situ Observation of γ^\prime Phase Transformation Dynamics During Selective Laser Melting of CMSX-4

Benjamin Wahlmann,* Erwin Krohmer, Christoph Breuning, Norbert Schell, Peter Staron, Eckart Uhlmann, and Carolin Körner

Additive manufacturing (AM) of superalloys has been attracting increasing interest. While most studies focus on the processability and mechanical properties of the finished product, it is also necessary to understand the phase transformations during the consecutive melting processes. Herein, the precipitation and dissolution of the γ' phase in the Ni-base superalloy CMSX-4 in a selective laser melting process is reported. These phase transformations are studied in situ by small-angle X-ray scattering (SAXS) during AM. Concurrent wide-angle X-ray scattering (WAXS) provides information on the evolution of lattice parameters and temperature during the process. Additional thermal and thermodynamic simulations are carried out to support the experiments. The investigations are focused on the influence of different beam scanning strategies as well as the effect of laser power and scanning speed on the phase transformation dynamics. Due to the high cooling and heating rates inherent to AM, phase transformations occur far off equilibrium. Both precipitation and dissolution of γ' phase are observed. The scan strategies are shown to have a considerable effect on the phase transformation dynamics, which exceed the impact of the beam parameters. The capability of combined SAXS and WAXS for the in situ study of phase transformations in AM processes is demonstrated.

B. Wahlmann, C. Breuning, Prof. C. Körner Chair of Materials Science and Engineering for Metals Friedrich-Alexander-Universität Erlangen-Nürnberg (FAU), Martensstr. 5, 91058 Erlangen, Germany E-mail: benjamin.wahlmann@fau.de

E. Krohmer, Prof. E. Uhlmann Institute for Machine Tools and Factory Management Technische Universität Berlin Pascalstraße 8-9, 10587 Berlin, Germany

Dr. N. Schell, Dr. P. Staron Institute of Materials Research Helmholtz-Zentrum Geesthacht Max-Planck-Str. 1, 21502 Geesthacht, Germany

The ORCID identification number(s) for the author(s) of this article can be found under https://doi.org/10.1002/adem.202100112.

© 2021 The Authors. Advanced Engineering Materials published by Wiley-VCH GmbH. This is an open access article under the terms of the Creative Commons Attribution License, which permits use, distribution and reproduction in any medium, provided the original work is properly cited.

DOI: 10.1002/adem.202100112

1. Introduction

Additive manufacturing (AM) offers new ways to fabricate high-performance alloys, e.g., nickel-base superalloys, for application in the hottest sections of jet engines or gas turbines. Powder-bed-based techniques such as selective electron beam melting (SEBM) or selective laser melting (SLM) allow great geometric design freedom and provide the ability to fine-tune microstructural properties by intelligent beam deflection and heat management. The microstructure can be tailored using appropriate combinations of scanning patterns, beam energies, and deflection speeds. Extensive effort has been directed at designing process parameters to tune the grain structures of titanium-, nickel-, and iron-base alloys.^[1–5] This has enabled the generation of microstructures ranging from equiaxed grains to single crystals. However, phase transformations that occur during AM processes have been investigated less.

In powder-bed-based AM processes such as SEBM or SLM, a component is built up layer by layer by fusing the metal powder selectively with an electron or laser beam. Therefore, a volume element is heated and then cools down repeatedly as the beam moves past the element over the powder bed multiple times. When further layers are added, the volume element is again reheated to consecutively lower peak temperatures, as more material is built up between the heat source and the considered volume element.^[6] This thermal cycling leads to repeated phase transformations involving successive nucleation, ripening, and dissolution processes. These transformations are inherently more difficult to observe than features on the grain size scale as a "post mortem" analysis at room temperature after the build is finished reveals only the final microstructural state but not the processes that created it. To better understand the phase transformations during processing, it is necessary to carry out in situ measurements.

In situ studies of laser-based AM have focused on the investigation of melt pool dynamics by high-speed X-ray imaging and on phase transformations studied by X-ray scattering. Imaging studies were generally conducted using preplaced powder on a solid substrate of the alloy of interest. The powder bed was confined by glassy carbon plates. Depending on the transmissivity of

www.aem-journal.com

ENGINEERING

the material, frame rates up to 50 kHz were achieved, allowing the monitoring of keyhole and pore formation and of powder and droplet spatter. Pores were shown to form due to the collapse of the laser-induced keyhole upon a change of the beam velocity. [7] Leung et al. studied melt track morphologies when processing Invar 36 with different parameters and developed a process map detailing the behavior of melt track morphologies in dependence of beam power and velocity. They also studied the melt track formation on an already melted layer. [8] Zhao et al. carried out simultaneous imaging and X-ray diffraction of Ti-6Al-4V powder and solid material. This allowed measurement of the solidification rate and monitoring of transformations between α and β phases during heating and cooling.^[9]

Pure time-resolved X-ray diffraction studies dealt with phase transformations in Ti-6Al-4V or tool steel during AM or rapid heating and cooling. Diffraction studies of X40CrMoV5-1 at 10 Hz during laser metal deposition revealed recurring austenitemartensite transformations in subsequent layers due to reheating by the laser beam. [10] Kenel et al. measured the β to α' transformation in Ti-6Al-4V during heating by a laser and subsequent rapid cooling at 1 kHz. These conditions were similar to those encountered during AM. [11] Hocine et al. also investigated phase transformations in Ti-6Al-4V. The experiments were carried out using a custom-built SLM device featuring a powder bed and at an acquisition rate of 20 kHz. This allowed the investigation of the effects of reheating in a single powder layer.^[12]

Several recent studies have focused on the processing of nickel-base superalloys by AM.[13,14] These alloys owe their extraordinary high-temperature strength to their microstructure consisting of 50%–70% of ordered intermetallic γ' precipitates (Ni₃(Al, Ti), L1₂ structure) embedded in a disordered y phase matrix. The γ' phase is stable up to nearly 1300 °C. However, due to their poor weldability, these alloys are prone to cracking and, thus, difficult to manufacture additively. In addition to hot or liquation cracking, hardening by precipitation of the γ' phase at high temperatures is suspected of contributing to the formation of cracks. [15,16] Therefore, detailed knowledge of the phase transformations induced by thermal cycling is necessary to optimize the processing conditions of superalloys.

In superalloys fabricated by SEBM, γ' particles exhibiting a gradient of sizes from tens to hundreds of nanometers are present after the building process.^[17] From the top to the bottom of a part, each layer is held at above 1000 °C for an increasing amount of time. This results in precipitates with increasing sizes. By contrast, in SLM-built parts, the temperature of the powder bed is often around 50-100 °C. Accordingly, cooling rates during the thermal cycles are higher, and precipitate growth is inhibited. In superalloys with a low γ^{\prime} phase fraction, no precipitates are found in the as-built state. [18] In alloys with a high γ' volume fraction, precipitates with sizes of several nm may be found, depending on the processing conditions.[19,20]

In a previous study, we investigated the transformation dynamics of the γ' phase in the nickel-base superalloy CMSX-4 while imposing a thermal profile similar to that occurring in SEBM, but with lower heating and cooling speed. [21] We proved that the precipitation of the γ^\prime phase is extraordinarily rapid and demonstrated the effect of heating and cooling cycles on dissolution and coarsening of the γ' phase. However, the phase transformations under real AM conditions have not yet been investigated. In this study, we conducted AM experiments using a SLM machine specifically designed for in-situ experiments.^[22] This allowed us to carry out measurements at different distances from the top layer within the built material. We carried out simultaneous small-angle and wide-angle X-ray scattering (SAXS/WAXS) measurements to clarify the evolution of γ' phase fraction and of lattice parameters during the manufacturing trials. This allowed us to link the thermal evolution to the transformations taking place at the same time. SAXS is especially useful in this case as the peak position of γ and γ' phase are nearly identical, making the use of WAXS difficult for phase identification. The experimental measurements are compared with simulations of temperature cycles and thermodynamic calculations of the γ' phase fractions.

2. Experimental Section

2.1. Experimental Setup

In this study, we conducted SLM experiments with the nickelbase superalloy CMSX-4 (composition: Ni-9.8 Co-6.4 Ta-6.5 Cr-6.4W-5.7 Al-2.8 Re-0.97 Ti-0.62 Mo-0.086 Hf, in wt%). The powder was produced by TLS Technik GmbH & Co. Spezialpulver KG by electrode induction-melting gas atomization with argon. To ensure a good flowability, only the size fraction from 105 to 150 µm was used.

The SLM machine used in the study is a modified version of the commercially available AconityMINI from Aconity3D GmbH. A detailed description of the machine was given by Uhlmann et al. [23] The custom process chamber was developed and built at Technische Universität Berlin. A single-mode continuous-wave ytterbium fiber laser, which emits a maximum power of 400 W at a wavelength of 1070 nm, served as the power source. At a working distance of 445 mm, the laser was focused to a diameter of about 60 µm. The powder bed had a size of $70 \times 1.5 \,\mathrm{mm}^2$ (length \times width). A mild steel plate was used as the substrate to support the powder bed. Each sample was built on a new plate. No substrate heating was applied. The powder bed was confined by glassy carbon plates with a thickness of 1 and 2.5 mm supplied by HTW Hochtemperatur-Werkstoffe GmbH. Before the SLM process was initiated, the chamber was flooded with argon. During the process, the oxygen level was kept below 2000 ppm. The process gas was circulated and filtered continuously to remove metal fumes. Inlet and outlet windows for the X-radiation were made of Kapton foils, which only minimally contributed to the X-ray scattering. An infrared pyrometer CTvideo 3MH2 from Optris GmbH was pointed at the middle of the powder bed to record the temperature profiles during scanning with the laser. The pyrometer measured the temperature within a circular area 1 mm in diameter. The measurable temperature range was 200-1500 °C.

The concurrent SAXS and WAXS measurements were carried out at the PETRA III facility at DESY at the high energy materials science beamline P07-EH3, operated by the Helmholtz-Zentrum Geesthacht. [24] A schematic of the setup is shown in Figure 1. The measurements were carried out using a photon energy of 79 keV (wavelength $\lambda = 0.01569$ nm). We found this to be a good compromise between photon flux and energy to

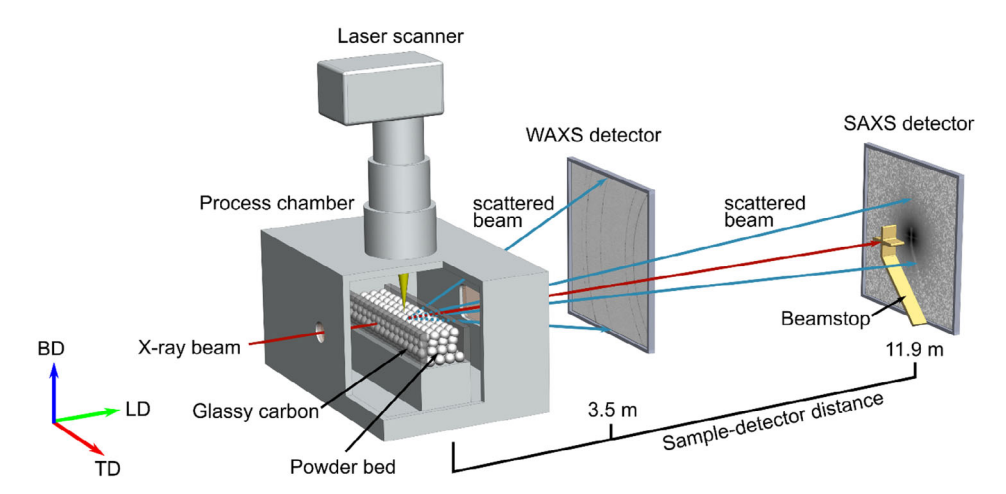


Figure 1. Experimental setup for in situ experiments at the beamline with the indication of LD, TD, and BD.

achieve a suitable transmission. A high intensity of the scattered beam was crucial for SAXS measurements to achieve a meaningful signal from the γ' precipitates. A cross-shaped beamstop with girders of 200 µm thickness combined with aluminum lenses that focused the synchrotron radiation beam allowed us to extend the range of scattering vectors \mathbf{q} ($\mathbf{q} = 4\pi \sin(\theta)/\lambda$ with the scattering angle 2θ and wavelength λ) down to $0.018\,\mathrm{nm}^{-1}$. The SAXS and WAXS patterns were collected on two Perkin Elmer XRD 1621 flat panel detectors (2048 × 2048 pixels, pixel size $200 \times 200 \ \mu\text{m}^2$). CMSX-4 strongly absorbs X-rays, making SAXS measurements at short exposure times challenging due to the low total signal from the γ' precipitates. As this study's goal is the in situ investigation of an AM process with a low characteristic time scale during which melting and solidification occur (down to 50-100 ms), the exposure time was set to 200 ms. We deemed this the best trade-off between temporal resolution and signal intensity. Higher flux would improve the detection of low amounts of γ' phase by SAXS, whereas faster acquisition would allow the monitoring of phenomena that occur during melting of single tracks.

For the concurrent in situ SAXS/WAXS measurements, the SAXS detector was placed 11.9 m from the sample, whereas the WAXS detector was located at 3.5 m distance. The WAXS detector was displaced out of the primary beam so as not to block the SAXS signal. The beam spot on the sample was roughly $0.2\times0.2~\text{mm}^2.$ As the layer height was $100~\mu\text{m}$, two layers are irradiated by the beam. It should be noted that the exposure time was longer than the aforementioned characteristic timescales of the AM process. That is why the recorded measurements should be viewed as the average of the state of the material during the exposure time and not as a momentary snapshot of the material's state, as, e.g., multiple heating and cooling cycles occurred during a single scattering measurement.

Further in situ WAXS measurements of CMSX-4 during heating with a rate of 5 $^{\circ}$ C s $^{-1}$ were conducted at P07-EH3 with a DIL 805 A D $^{-1}$ dilatometer by TA instruments modified for synchrotron measurements. $^{[25]}$ This allowed us to determine the lattice parameter of CMSX-4 in dependence of temperature and to infer the approximate temperature of the gauge volume from the in situ WAXS measurements.

Ex situ WAXS measurements of the as-built material were carried out at the beamline P21.2 using a beam energy of 69 keV and a Varex XRD 4343CT detector (2880 \times 2880 pixels, pixel size $150\times150\,\mu\text{m}^2$) to characterize the distribution of phases in the build direction (BD) in the final state.

2.2. Experimental Procedure

Numerous parameters determined the quality and microstructure of additively manufactured parts. In this study, we varied three parameters: beam power P, scan speed ν_s , and the scanning pattern. These governed the thermal history of the process and, thus, the kinetics and dynamics of phase transformations. We chose a simple geometry to emphasize the very fundamental transformation mechanisms. The samples were thin walls with a thickness of 1.5 mm and a width of 40 mm.

The scanning patterns were kept simple, as well. We used two patterns, both consisting of unidirectional scans: one in the direction of the synchrotron radiation beam (longitudinal direction [LD]) and one in perpendicular orientation (transverse direction [TD]) (Figure 2a). Accordingly, the scan lengths, i.e., the length of one melt line, are 40 mm for transverse scans. For longitudinal scans, the scan length was 1.0 mm to avoid heating of the glassy carbon plates by the laser. However, as the melt pool size exceeded the scanned area, all the powder in the LD was molten except for a few single particles. The hatch distance was 50 µm. This ensured that the laser would irradiate the surface entirely without leaving any gaps. The time required for one line to be melted was proportional to the scan length for a constant scan speed. This resulted in a more concentrated heat input for short scan lengths. Therefore, the thermal history depended greatly on the chosen scanning pattern, even if the total heat input was not changed.

The beam power was varied in the range of $120-308 \, \text{W}$, whereas the scan speed ranged from 300 to $700 \, \text{mm s}^{-1}$. The complete set of parameters is shown in **Table 1**. Some parameters were chosen to study the effects of total heat input at constant P/v_s (called line energy, E_{L_s} in the following); others were adapted from parameters used in SEBM of CMSX-4.

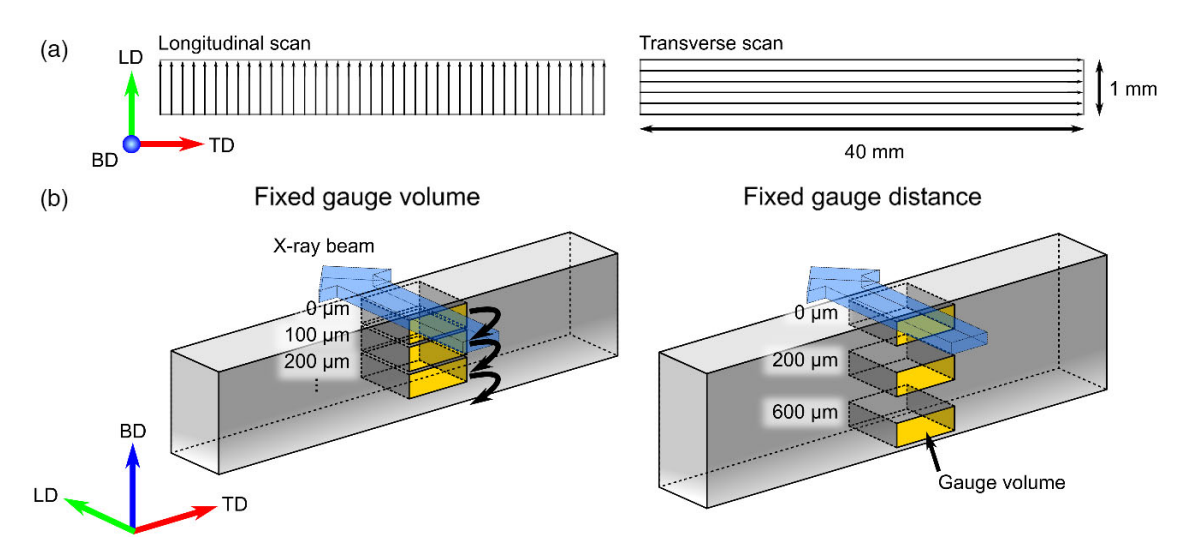


Figure 2. In situ experimental procedure and measurement modes. Dimensions are not to scale. The LD, TD, and BD are the same as in Figure 1. a) Patterns of longitudinal and transverse laser scanning modes, b) Schematic representation of measurement modes. In fixed gauge volume mode, the gauge volume's distance from the sample surface is increased by the layer thickness after building each layer. In fixed gauge distance mode, the gauge volume has a fixed distance from the upper sample surface.

Table 1. Process parameters (L = longitudinal, T = transverse scanning pattern).

Power [W]	Scan speed [[mm] [s] ⁻¹]	Line energy [J [mm] ⁻¹]	Scanning pattern
120	300	0.4	Т
120	500	0.24	L
200	500	0.4	L, T
274	513	0.53	L, T
280	700	0.4	L, T
308	570	0.54	L, T

The measurements were carried out in two modes (Figure 2b). In fixed gauge volume mode, a single volume element was traced while building 11 consecutive layers. Starting at the upper sample edge, the maximum distance of the probed volume to the edge was 1000 µm. As the substrate was lowered relative to the process chamber after each layer was molten, the entire SLM machine must be lifted by the same amount. For this purpose, the machine was placed on the heavy load hexapod at P07-EH3, which allowed six-axis movements with a precision of 1 µm. In the fixed gauge distance mode, the sample was probed at fixed distances (0, 200, and 600 µm) from the upper sample surface while melting multiple layers.

2.3. Data Analysis

The SAXS patterns were corrected for background from the instrument and the glassy carbon plates confining the powder bed. All patterns were integrated azimuthally with the program DPDAK. [26] A time series of integrated SAXS and WAXS data collected in the fixed gauge volume measurement mode for longitudinal and transverse scanning patterns is shown in Figure 3.

The SAXS scattering curves were corrected individually by removing the isotropic background from incoherent scattering, as described by De Geuser and Deschamps.^[27] In theory, particle sizes, shapes, and distributions could be determined from the scattering curves. In this case, however, the contribution of scattering from the γ' precipitates to the total scattered intensity was too low to determine these features reliably. For the largest part, the scattering signal was likely caused by the matrix or inhomogeneities caused by cellular segregation during solidification. The integrated intensity Q_0 allowed the calculation of the fractions of scattering phases. In the case of two phases, it was related to the volume fraction ϕ of the scatterers by the relation $Q_0 = 2\pi^2 (\Delta \rho^2) \phi (1 - \phi)$, where $\Delta \rho$ is the contrast between the phases. Q_0 was determined by integrating the product of intensity I and the squared scattering vector, $\mathbf{q}^2I(\mathbf{q})$. We limited the integration range to $q_{\min} = 0.018 \text{ nm}^{-1}$, set by the shadow of the beamstop, and $q_{\text{max}} = 0.30 \,\text{nm}^{-1}$, where the intensity falls down to the remaining background noise. The approximate integrated intensity Q' is evaluated as

$$Q' = \int_{q}^{q_{\text{max}}} q^2 I(q) dq. \tag{1}$$

This measure played a key role in our analysis of phase transformations. Q' consistently underestimates Q_0 ; for qualitative analysis, though, the difference was negligible. The relation shown earlier allowed the determination of phase fractions if the scattering contrast, i.e., the difference in the phases' electron density, was known. As the phase compositions were temperature dependent, they were difficult to determine experimentally and are usually subject to considerable uncertainty. Furthermore, in this study, multiple scatterers— γ' , γ , and liquid phase contributed to the intensity. Quantitatively accurate analysis required separating the individual contributions. Thus, we limited ourselves to a qualitative analysis. As we showed earlier for

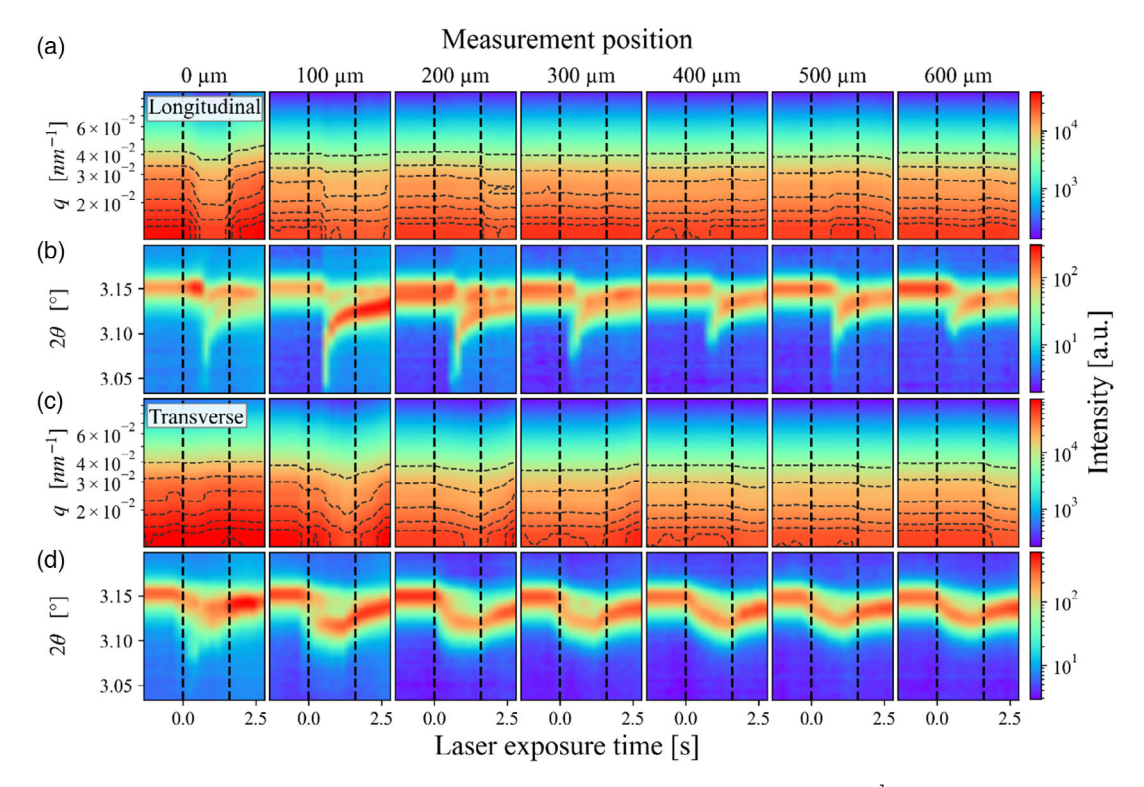


Figure 3. Background-corrected and integrated a,c) SAXS and b,d) WAXS data, collected at 200 W/500 mm s⁻¹. The measurements were carried out in fixed gauge volume mode with a,b) longitudinal and c,d) transverse scanning patterns. Isointensity lines in the SAXS plots serve to enhance subtle changes in intensity. The vertical dashed lines indicate the time during which the laser is active. Scattering vectors and angles are represented by q and θ . The 111 reflection is shown in (b) and (d).

the alloy CMSX-4, an increase or decrease in Q' could be related to an equivalent change in the γ' phase fraction. These changes were quite subtle for the most part (Figure 3a, c). In addition, differences in density between metal powder and the solidified material lead to differing absolute values of Q'. To enhance the changes in Q', the calculated values were normalized with respect to the value of Q' measured before the melting started. As the powder was molten entirely, except for the uppermost layer, γ' precipitates from only the solid material contribute to Q'.

The WAXS patterns did not undergo further image correction steps, as we only determined the peak positions. The WAXS profiles (Figure 3b, d) were fitted with pseudo-Voigt functions to determine the peak positions of the γ phase. As the lattice parameters of γ and γ' phases were nearly identical, they could not be separated. However, the evolution of the peak positions allowed us to determine the influence of scanning patterns on the thermal history during the process qualitatively. The grain size of the as-built material was comparatively large with respect to the gauge size so that the grains in Bragg condition produce spotty diffraction patterns. Therefore, we integrated the diffraction patterns over the entire azimuthal range covered by the detector to achieve adequate grain statistics (cf. Figure 1). Thermal strains were different in build and TDs, leading to slightly differing lattice parameters.^[22] Consequently, the lattice parameters determined here were the average of the parameters subject to different strains. As the WAXS detector was positioned to the left of the primary beam, we mainly observed lattice shifts in the TD. The intensity of the peaks during scanning of the first layer was lower than the intensities during the subsequent scans due to the presence of liquid phase in the gauge volume.

3. Results

3.1. Microstructure

The as-built state of the material is the starting point for analyzing in situ phase transformations (**Figure 4**). The samples exhibit numerous intergranular cracks typical for nonweldable superalloys fabricated by AM at low powder bed temperatures. These form probably due to hot cracking induced by liquation of grain boundaries when the material is reheated and due to residual stresses. The grains contain a cellular or cellular-dendritic solidification substructure with an average size of $1\,\mu m$. An unmelted powder particle that was attached to the sample is shown in the right panel of Figure 4. The dendrites present in the powder are about $10\,\mu m$ wide, which is an order of magnitude larger than the cells in the as-built material.

Due to the extremely fast solidification speed in SLM, the formation of γ' precipitates, albeit very fast due to the little reordering required to form the ordered Ni₃(Al, Ti) compound, is suppressed for the most part. In SLM-built nickel-base



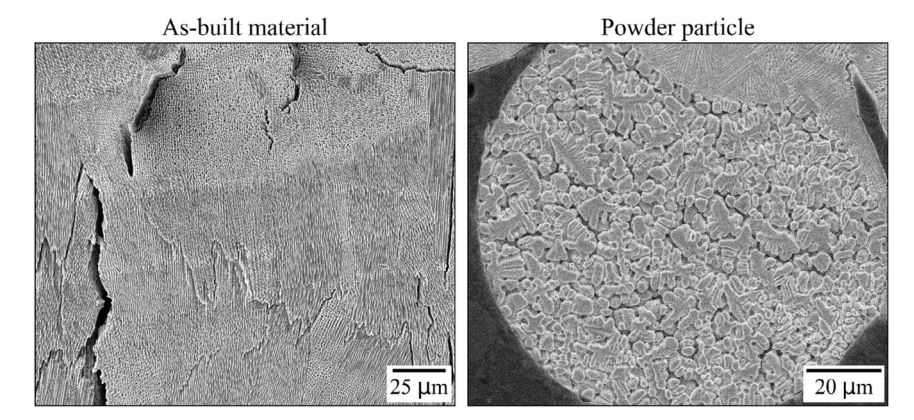


Figure 4. Microstructure of as-built samples and an unmelted powder particle attached to the sample. Due to the fast solidification, the SLM-built material's cellular structures are about one-tenth of the size of the dendrites found in the metal powder particle. The as-built sample shows numerous solidification cracks.

superalloys, γ' is either present in the form of particles only a few nm in size or is not observed at all. [19,20] Furthermore, recent atom probe tomography investigations of a single superalloy powder particle showed the absence of γ' phase as well. [28] By contrast, high amounts of γ' phase are typically found in SEBM-built Ni-base superalloys due to the extended holding time at the building temperature of about 1000 °C. [17]

Samples produced by longitudinal and transverse scanning were examined by ex situ WAXS from the CMSX-4/substrate interface to a distance of 4 mm from the interface (Figure 5). The peaks of γ and γ' phases overlap, as the phases' lattice parameters differ only by less than a percent. No superstructure reflections of the γ' phase were found. At the interface, several peaks could be attributed to the α -phase of the steel substrate. Different relative intensities of the γ peaks are caused by the texture of the samples, which are strongly textured in the BD. Furthermore, the grains are comparatively large in proportion to the X-ray beam gauge size.

Due to its ordering, the γ' phase exhibits superstructure reflections such as 111 or 210 reflections with low intensity. However, such superstructure reflections could not be identified unambiguously against the background. This is also the case for WAXS measurements of the powder (not shown here). Therefore, the existence of γ' phase in the as-built state could not be confirmed by the WAXS measurements. This, however, does not preclude the formation of small amounts of γ' phase during the AM process.

3.2. Simulation of Temperature Evolution

Diffusion-dependent phase transformations are primarily governed by the thermodynamic driving force, i.e., the difference of the Gibbs Free Energy between the transient and the equilibrium state, and the kinetics of the transformation, which are determined by the diffusivity of the constituting species.

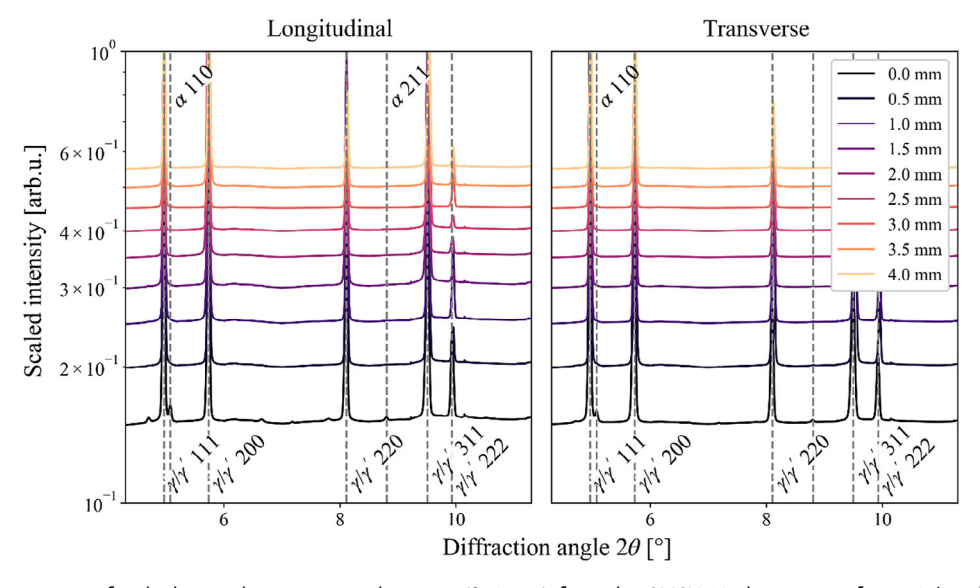


Figure 5. Diffraction spectra of as-built samples at various distances (0–4 mm) from the CMSX-4/substrate interface. γ/γ' -peaks are attributed to CMSX-4, the α-peaks to the substrate. The intensities were scaled and normalized with respect to the highest value in each spectrum.

www.aem-journal.com

www.advancedsciencenews.com

These factors are strongly dependent on temperature. Thus, an understanding of the temperature distribution within the sample and evolution is necessary to interpret the SAXS measurements. The thermal simulations are based on a semianalytical approach, implementing a transient solution of a volumetric Gaussian heat source, which is an extension of the classical Rosenthal model. [29,30] Here, the heat equation is solved by integrating the temperature field created by a heat source active for a differential time period in time at each grid point. The analytical integration of the solution is prohibited by the piecewise definition of the scan paths; therefore, a Gaussian quadrature scheme, proposed by Stump and Plotkowski numerically integrated the temperature at a given time and location.^[31]

The model approximates the sample as a semi-infinite medium with constant material parameters. Only heat transfer by conduction is considered. Consequently, this model's solutions are less accurate than, e.g., a full finite element simulation incorporating phase change and heat transfer by radiation; however, they allow a qualitative assessment of thermal profiles.^[32] Furthermore, as the temperature can be computed independently at each point of the simulation domain, the simulation domain's spatial resolution can be chosen independently of the beam diameter. This enables efficient simulations in large domains. This approach has been applied successfully to the modeling of electron beam and laser melting of a nickel-base alloy.[33]

Two exemplary parameter combinations were chosen for further examination in detail: a longitudinal scanning pattern with a beam power of 120 W and a scanning speed of $500\,\mathrm{mm\ s^{-1}}$ as well as a transverse pattern with $280\,\mathrm{W}$ and 700 mm s⁻¹. For these parameters, the WAXS patterns had the highest quality over the entire measurement, which allowed deduction of the temperature evolution from the lattice parameters (cf. Section 2.1). The evolution of the temperature in the samples was simulated for these parameters (Figure 6). The longitudinal pattern results in a persistent melt pool, which is dragged in the TD across the sample surface. This melt pool geometry arises when the beam return time, i.e., the time required to scan a single line, is so short that the melt cannot solidify entirely until the next line is melted. As a result, a large melt pool is formed that spans over the entire sample in LD. Notably, the base material remains at ambient temperature until the laser beam hits the observed volume. The material cools slowly as the laser beam passes. The melt pool has a depth of 0.32 mm.

In a transverse pattern, each melt track is carried across the sample surface in the TD. The melt pool is long and narrow and, with a depth of 0.26 mm, shallower than for the longitudinal scan strategy, even though the line energy is higher (0.4 vs 0.24 J mm⁻¹). Figure 6 also demonstrates that the entire sample is heated slowly but more evenly than with a longitudinal scan pattern. Furthermore, the sample reaches higher temperatures at a greater depth. Thus, it is apparent that the scanning strategy has a significant impact on the thermal history imposed on the sample. The influence of the scanning pattern on the temperature profile is greater than that of the beam parameters for the parameters covered in this study.

In the case of longitudinal scanning, the calculated melt pool size is significantly larger than those typically observed in single line scans. For the nickel-base alloy Inconel 718, a melt pool length and width of around 0.4 and 0.2 mm, respectively, would be expected.^[34] As multiple melt lines are placed next to each other in this setup, we expect a cumulation of heat, leading to the development of a larger melt pool. The simulated melt pool has a length of 5 mm and moves with a speed of 25 mm s⁻¹ in TD. Therefore, the melt pool would cross the gauge volume within 0.2 s. We compared the average simulated temperatures in the gauge volume, the pyrometer measurements, and the temperatures inferred from dilatometer measurements of CMSX-4

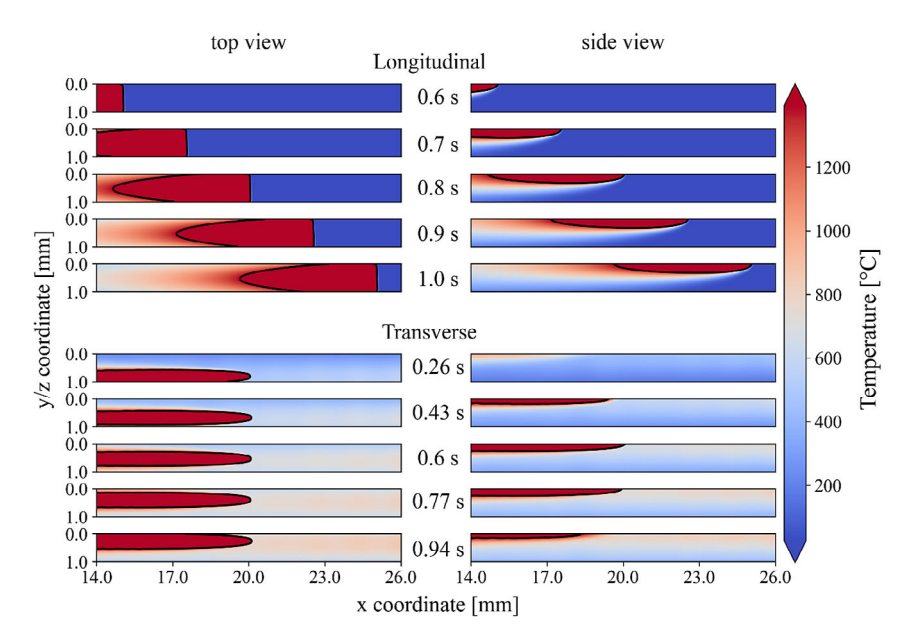


Figure 6. Simulated temperature distribution during the melting of one layer for exemplary parameter combinations (longitudinal: $120 \, \text{W}/500 \, \text{mm s}^{-1}$, transverse: 280 W/700 mm s⁻¹). A contour line delineates the melt pool. The color scale is capped at the melting temperature of CMSX-4.



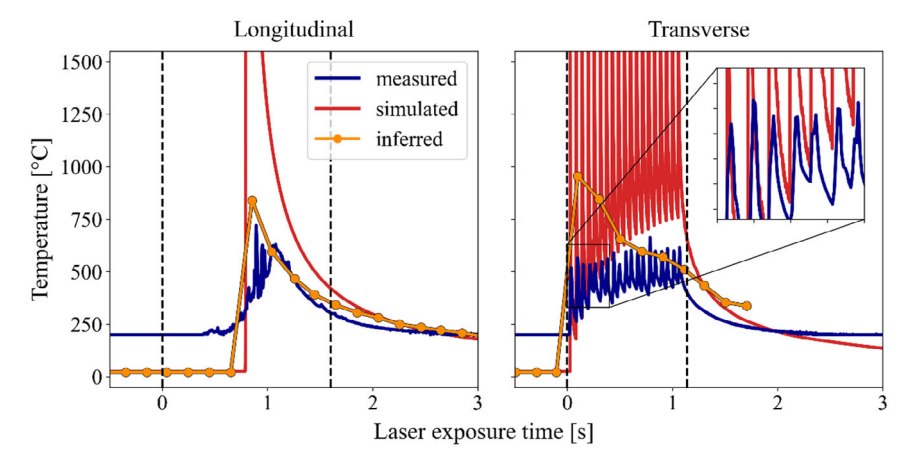


Figure 7. Simulated temperature in the gauge volume at the top layer, measured pyrometer temperature curves, and temperatures inferred from the lattice parameters measured in the top layer for the parameter combinations from Figure 6. The vertical dashed lines indicate the time during which the laser is active

to assess the accuracy of the simulation (**Figure 7**). The simulated temperature was averaged within the gauge volume to consider that WAXS and SAXS effectively measure the average properties in the gauge volume. The pyrometer was calibrated with an Inconel 625 sample, another Ni-base alloy. Its temperature was measured with a Type K thermocouple. A precise calibration would require knowledge of the emissivities of bulk material, powder, and liquid phase. Therefore, the absolute measured temperatures may not be accurate.

However, it is evident that the widths of the simulated and measured temperatures are quite similar for both scanning patterns. The earlier onset of the measured temperature peak and the overall lower measured temperature in the longitudinal scan may be caused by the pyrometer spot size, which is much greater than the gauge volume. Therefore, the temperature is averaged over a greater area than in the simulation. Furthermore, the pyrometer only records temperature changes above 200 °C. The similarity of the curves allows us to conclude that the melt pool lengths are represented fairly accurately by the simulation. Considering the transverse scanning, both simulations and measurements show the same principal features: short temperature spikes corresponding to each scan and a steady increase in temperature during the melting of the powder layer. The melt pool depths were measured using micrographs to \approx 240–340 µm (longitudinal) and 180-220 µm (transverse scans). Thus, the measured melt pool depths are lower than the simulate ones, but are still in fairly good agreement.

Furthermore, the inferred temperatures show a good agreement with the pyrometer measurements of the longitudinal scan. At the beginning of the transverse scanning the inferred temperature is higher than the measured temperature, which may be related to uncertainties in the peak position due to spotty diffraction patterns and less distinct peaks (cf. Section 2.3). Overall, the simulated temperatures are higher than the experimentally determined ones. This may be caused by the lack of heat transfer by radiation or of latent heat in the semianalytical model. In summary, the simulated temperatures are realistic enough to predict the temperature evolution at greater depths in the material.

3.3. Evolution of γ' Phase in Single Layers

The changes in Q' allow us to obtain a general understanding of the phase transformations that occur in different depths in the sample during the manufacturing process (**Figure 8**). The diagram shows the parameter combinations of laser beam power and scan speed, as well as the maximum percentual changes in Q' during the laser exposure in relation to the value of Q' before the exposure of the layer started. For each parameter combination, the maxima and minima of 10 measurements in fixed gauge distance mode were averaged.

Three phases can be present in the alloy during the in situ AM experiments: the γ matrix, the γ' phase, and the liquid phase. The liquid phase has the same chemical composition as the solid but a lower density; therefore, we expect a slightly lower electron density than in the solid γ phase.^[35] Consequently, there is only a small scattering contrast between liquid and γ phase, leading to a small value of Q'. Furthermore, when the sample melts, all inhomogeneities in the solid are dissolved, which reduces the overall variation of electron densities in the gauge volume and, thus, Q'. In conclusion, melting causes a decrease in Q'.

As stated in Section 2.2, increases in Q' can be related to an increase in the γ' phase fraction. Given that no γ' phase could be identified by WAXS, γ' formation was likely limited to very small amounts. It is also possible to detect the early stages of a phase transformation before a phase is detectable by WAXS. [36] In this case, an ordering reaction from the γ (A1) to the γ' (L1₂) phase will arise on a short range from chemical fluctuations. [28] As different phase transformations can have similar effects on Q', the occurring transformations cannot be inferred unambiguously from the Q' variations. The following analysis, therefore, relies on the previous thermal simulations to properly relate the phase transformations to the in situ SAXS measurements.

In the uppermost layer (0 μ m), significant decreases in Q' of about 30 % are observed in longitudinal scanning mode, while only small increases occur. This behavior implies that the powder is melting, as no γ' is present in the material at this stage. Conversely, in transverse mode, Q' increases and decreases

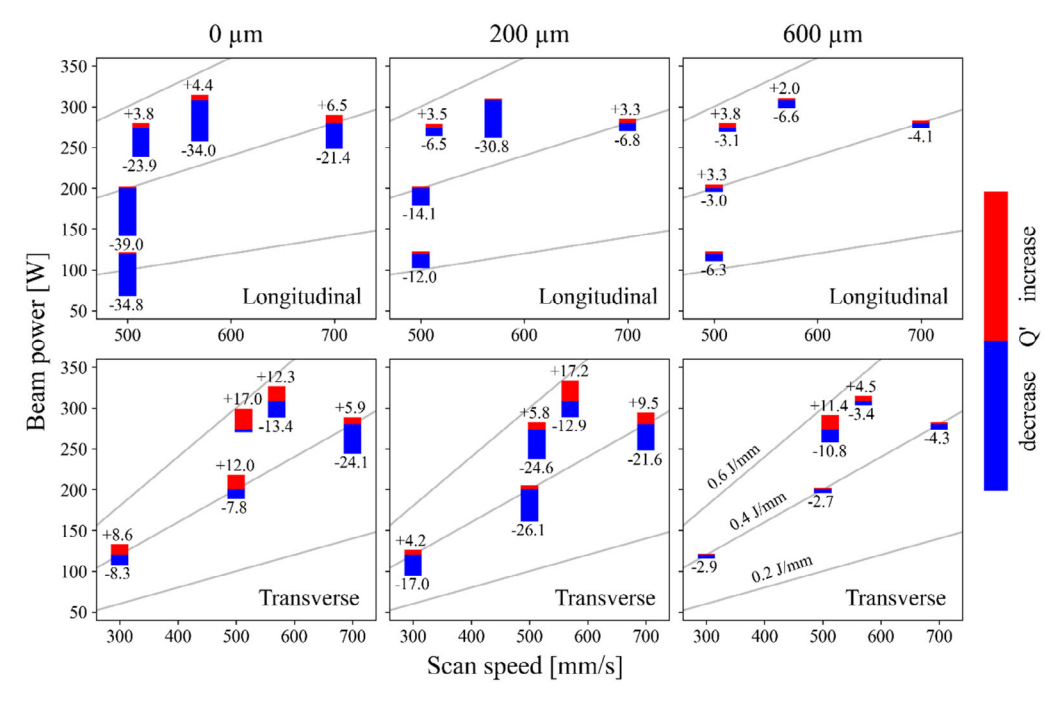


Figure 8. Relative changes in Q' during melting for longitudinal and transverse scanning patterns. The diamond symbols represent the beam power and scan speed, whereas the blue and red bars indicate the maximum decrease (primarily due to melting) and increase (primarily due to γ' phase formation) in Q'. The magnitude of the changes is given in percent. The gray lines indicate parameters of constant line energies E_L .

are for the most part equally large. The increase in Q' possibly indicates the formation of γ' phase. The γ' phase likely formed in the powder before the melting and in the just solidified material, which retains a high temperature.

About 200 μm below the surface, the trend is generally the same. With a longitudinal scanning pattern, Q' still decreases during laser exposure, albeit less significantly. This can mainly be attributed to the melting of the sample, since, according to the thermal simulations (Figure 6), the melt pool extends well into the monitored domain. In the case of a transverse pattern, both significant increases and decreases in Q' can be observed. Considering that the previous simulations predicted that the sample was heated evenly, we can deduce that the γ' phase first formed during this heating stage, followed by the melting of the alloy.

At a depth of 600 μ m, all relative changes are less substantial, given the lower peak temperatures at a greater distance from the melt pool. Increases and decreases in Q' are of about equal magnitude. As the melt pools are predicted not to extend this far, melting is not expected to influence the Q' changes. Hence, we attribute these changes purely to the formation and dissolution of the γ' phase or to early stage ordering/disordering reactions.

As the phase transformation kinetics are strongly dependent on temperature and heating or cooling rates, a dependence of Q' on the heat input, characterized by the line energy $E_{\rm L}$, is expected. However, the inherent uncertainties of the SAXS measurements caused by the small γ' phase fraction, short exposure times, and strong X-ray absorption of the CMSX-4 alloy overshadow any possible dependencies, so that no clear trend can be determined. Instead, the effect of the scanning patterns is predominant.

3.4. Evolution of γ' Phase in Consecutive Layers

The combination of SAXS and WAXS measurements in fixed gauge volume mode allows us to examine phase changes and their kinetics in detail throughout the building process. This analysis is carried out for longitudinal (**Figure 9**, parameters: $120 \, \text{W}/500 \, \text{mm s}^{-1}$) and transverse (**Figure 10**, parameters: $280 \, \text{W}/700 \, \text{mm s}^{-1}$) scanning patterns. Therefore, we consider the normalized Q' measure and the status of the laser (top panels) as well as the lattice parameters obtained from the 111 reflection and the profiles of the average simulated temperature in the monitored volume (bottom panels). The measurements were carried out from the sample surface up to a depth of 1 mm. Due to the normalization, the Q' curves should be interpreted only with regard to the features in single panels.

Regarding the longitudinal pattern (Figure 9), in the first three layers, drastic reductions in Q' occur after half of the laser's active time has elapsed, as the gauge volume is in the middle of the sample. The rapid declines reflect the fast heating in longitudinal scanning mode. Starting from a depth of 300 μ m, the steepness of these decreases is reduced continuously. As the thermal simulations yield a melt pool depth of 0.32 mm, we can attribute the reductions in Q' primarily to the melting of the sample. At greater depths, the synchrotron radiation beam gauge partially covers molten and unmolten material. As the irradiated volume spans over two layers, the SAXS signal contains contributions from both material states, which alleviates the sharp drop of Q'.

From 400 μm depth onward, the Q' profiles feature slight but consistent growth before each drop. These could stem from the

SCIENCE NEWS ______

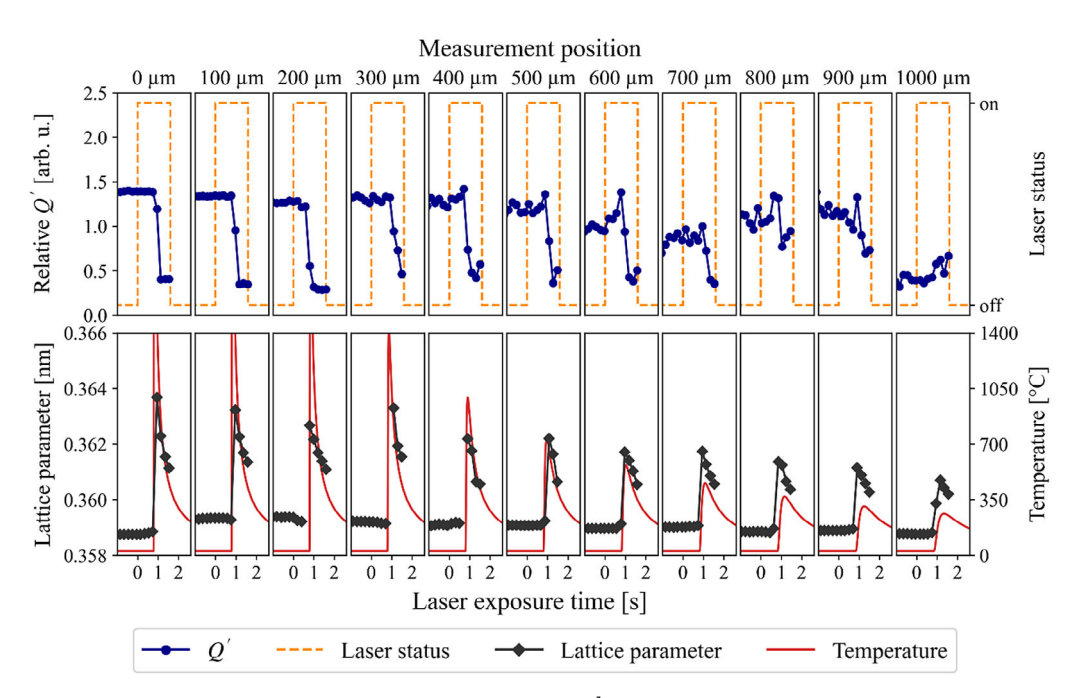


Figure 9. Longitudinal scan in fixed gauge volume mode at 120 W and 500 mm s⁻¹. The top panels show the evolution of Q' (blue) and the laser status (orange), the bottom panels depict lattice parameters (gray), and the simulated temperature profiles.

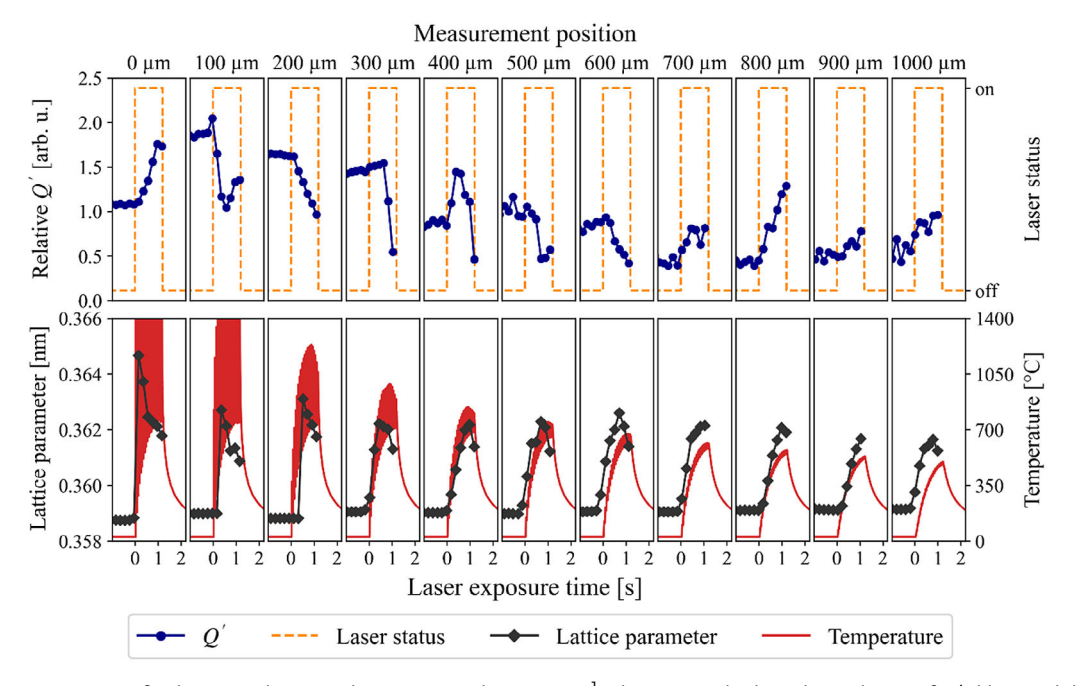


Figure 10. Transverse scan in fixed gauge volume mode at 280 W and 700 mm s⁻¹. The top panels show the evolution of Q' (blue) and the laser status (orange), the bottom panels depict lattice parameters (gray), and the simulated temperature profiles.

formation of γ' from the γ phase, similar to the formation of γ' phase in the powder for the transverse scanning mode (Figure 8). This reaction takes place as soon as the material is heated. In turn, the following decline is induced by the dissolution of γ' , as higher temperatures are reached. Melting is unlikely to affect Q' in this case as the thermal simulations show that melting occurs without significant prior heating, which would allow

the formation of the γ' phase. Shortly before the laser is turned off, a slight increase in Q' hints at the recurring formation of γ' , which occurs during the cooling stage. As demonstrated in the bottom panels, the cooling rate is significantly slower than the heating rate, whereby the material remains at an elevated temperature for a sufficient amount of time to allow for the formation of the γ' phase.



The lattice parameters are subject to thermal expansion and residual stresses. It is assumed that the contribution of the thermal expansion outweighs the mechanical strains as the Young's modulus decreases with higher temperature. Therefore, the evolution of lattice parameters can be employed to assess if the simulations reflect the actual thermal history appropriately. The peak lattice parameters steadily decrease from the sample surface downward, which conforms to the simulated thermal history. However, within the upper four layers, no significant differences in the evolution of the lattice parameters are noticeable. Multiple effects cause this behavior: as sharp reflections are only obtained from the solid phases, the liquidus temperature of CMSX-4 poses an upper limit to the measurable lattice parameter. Furthermore, the heating rate is too high to be resolved by the exposure time of 200 ms. Rather than the momentary lattice parameter, the measurements represent the parameters' average over the exposure time.

The Q' curves of the transverse scanning strategy (Figure 10) display several differences in comparison with the longitudinal pattern. At the sample surface, Q' rises as soon as the melting starts due to the formation of the γ' phase in the powder and the as-solidified material. While each line is molten, the neighboring material is heated to a sufficiently high temperature to form the phase. In the following layers, both the growth and decline of Q' are observable. While we attribute the growth again to the formation of γ' phase, the decline in the upper layers is most likely caused by melting and γ' dissolution. The mechanism that leads to these phase transformations is the same as in the uppermost layer. However, as the peak temperatures in these layers are lower than in the top layer, γ' forms more slowly.

At 700 μ m depth and below, Q' strictly increases during the melting of the sample surface. The thermal simulations

demonstrate that the material retains a higher temperature for a longer duration than for the longitudinal scanning pattern. Accordingly, the formation of γ' is promoted more strongly.

The lattice parameter evolution qualitatively matches the simulated temperatures well from 400 μm onward. At lower depths, the initial rates of change of the lattice spacing and, thus, the apparent heating rates are higher than predicted. It should be noted, though, that close to the melt pool, each passing of the laser beam induces a temperature spike with a duration of about 0.06 s (cf. Figure 7), leading to multiple cycles of extremely fast heating and cooling. These spikes are responsible for the filled areas in the temperature plot of Figure 10, as they cannot be resolved in the plot. These temperature cycles cannot be captured by the WAXS measurements, whereby the measured lattice parameters may not accurately represent the temperature of the gauge volume.

4. Discussion

During the SLM process, the phase transformations are subject to highly nonequilibrium processes induced by the extraordinarily fast heating and cooling rates. To verify the temperature simulations, we inferred the temperature in the gauge volume from lattice parameters using in situ WAXS measurements of CMSX-4 with a dilatometer at a controlled heating rate. Figure 11 shows the simulated temperatures for the previously examined parameter sets (Figure 9 and 10) and the corresponding temperatures calculated from the lattice parameters. The characteristic features of both temperature profiles—nearly instantaneous heating for the longitudinal scanning pattern and a gentler rise in temperature for the transverse pattern—are

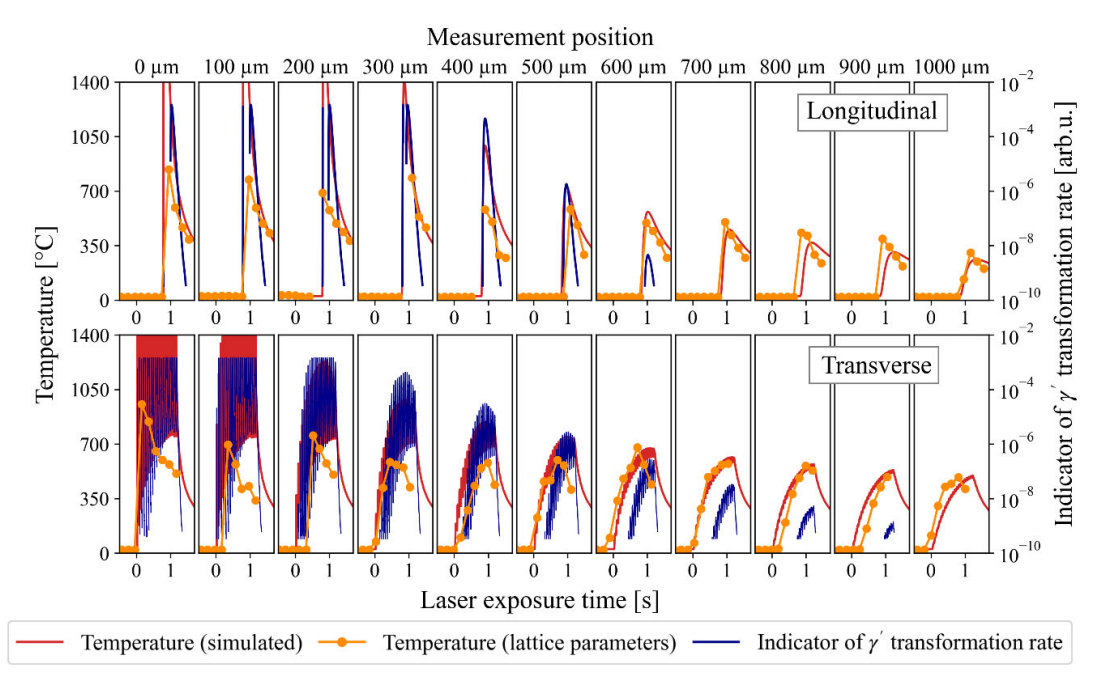


Figure 11. Analysis of γ' formation. The transformation speed indicator is calculated as the product of the driving force for the formation of γ' from the supersaturated γ phase and the diffusivity of Al in the matrix. Both measures are normalized with regard to their values at the γ' solvus temperature. The simulated temperatures coincide well with the temperatures inferred from the lattice parameters.

www.aem-journal.com

represented well. At $500\,\mu m$ and further, the peak temperatures also match the predictions. At lower distances to the sample surface, the discrepancies are more significant. This may be caused by the comparatively low temporal resolution of the WAXS measurements and a significant contribution of radiation to the heat transfer, which is not included in our semianalytical model. Overall, however, the simulated temperature evolution is accurate enough to serve as the starting point for discussing the mechanisms governing the nonequilibrium phase transformations.

Phase transformations are induced by driving forces and controlled by the diffusivities of the relevant species. [37] In this study, the as-solidified material consists solely of the γ phase. In thermodynamic equilibrium, CMSX-4 consists of roughly 70 % γ' phase embedded in the γ matrix. Therefore, in this study, after solidification, the matrix is in a supersaturated state. The driving force for the formation of γ' can be represented as the Gibbs free energy difference between the supersaturated and the equilibrium state. [38] As the equilibrium fraction of γ' phase grows with decreasing temperature, so will the driving force.

In addition to the principal element Ni, the γ' phase is mainly constituted of Al, whereas the other alloying elements are present in fractions of less than 5 %. As a first-order approximation, the rate of the γ' transformation can be assumed to be controlled by the diffusivity of Al in the supersaturated γ phase. The diffusivity, being thermally activated, increases exponentially with temperature.

In case of nucleation and growth, the reduction in energy due to the phase transformation must outweigh the increase in surface energy to form stable particles. As the surface energy of γ' precipitates is very low (typically around 0.01 J m⁻²), this contribution was neglected. [39] We defined an indicator of phase transformation rate as the product of the driving force of transformation from γ to γ' and Al diffusivity. As these measures are of different orders of magnitude, both were normalized with respect to the values at the γ' solvus temperature (1298 °C). The calculations were carried out with the Thermo-Calc software package version 2020a, including the diffusion module DICTRA, with the databases TCNI9 and MOBNI5. [40] The properties were only calculated down to a bottom temperature of 500 °C, as the database reliability diminishes below this threshold. This, however, does not imply that phase transformations or ordering reactions could not take place at lower temperatures. The Q' curves suggest that γ' continues to form, as the absolute values of Q' are always higher before melting than afterward. The resulting curves are presented in Figure 11.

According to this analysis, the γ' transformation rate is highest at 1130 °C. Two significant differences are evident comparing the transformation rates for longitudinal and transverse scan patterns: first, the transverse scanning strategy leads to higher transformation rates, especially at greater depths in the sample. Second, for transverse scanning, the transformation rate is higher for a longer total duration.

The phase transformation rate reaches a maximum just after the beginning of the melting for transverse scanning in the upper layers. This is reflected in the Q' curves of the first two layers (Figure 10), where pronounced rises of Q' are apparent. Conversely, in the case of longitudinal scanning, up to a depth of 400 μ m, the laser heats the sample to the melting temperature of 1346 °C (as calculated with Thermo-Calc) almost instantly. This does not allow for any formation of the γ' phase before

melting. The lower layers of the transversely scanned sample at 700 μm and further reach significantly higher γ' transformation rates than for longitudinal scanning due to the more even heating, as shown in Figure 6. Although the difference in peak temperatures is only 100–200 °C, the Al diffusivity's exponential temperature dependence leads to a considerably accelerated phase transformation rate.

It should be noted that the indicator of γ' transformation rate varies by several orders of magnitude due to the exponential temperature dependence of Al diffusivity. Consequently, the state of the material should be dominated by transformations within the first few layers. However, as we make strongly simplified assumptions, the actual γ' transformation rate should not be considered directly proportional to the calculated indicator. This only serves to qualitatively explain the variations of transformation dynamics induced by the different process parameter combinations.

In addition to the formation of the γ' phase, we must also consider its dissolution to understand the phase transformations during the SLM process. A full quantitative analysis would require detailed simulations of the nonequilibrium transformation processes. That is beyond the scope of this study. Instead, we will limit ourselves to a purely qualitative estimation. Considering the simulated melt pool depths (Figure 6), we can assume that dissolution of the γ' phase occurs between a depth of 400 and 900 μ m for longitudinal scanning and between 300 and 600 μ m for transverse scanning. In these regions, the diminishing of the γ' phase is the most likely phenomenon-that could explain the decrease in Q'.

The composition of the γ' phase off equilibrium is not known. We can, however, assume that it is less enriched in γ' -stabilizing elements (Al, Ti, Ta) than in the equilibrium state since the rapid solidification conditions permit only little diffusion. This would lead to a lowered solution temperature of the γ' phase. Thermo-Calc calculations show that such off-equilibrium γ' phase can dissolve to a noticeable degree, even though the maximum temperatures reached in the regions mentioned earlier are far below the equilibrium γ' solvus temperature.

The γ' phase transformations differ strongly in dependence of the cooling rates. In situ SAXS measurements of CMSX–4 under cyclic heating and cooling with rates of 200–300 °C s $^{-1}$ showed that, in contrast to this study, the γ' phase was not far from the equilibrium state. $^{[21]}$ During both cooling and heating, the transformation rates were equal. When cooling from subsolvus temperatures, the presence of γ' nuclei facilitated the precipitation. Cooling to room temperature led to a γ' phase fraction close to the predicted equilibrium fraction. In this study, cooling rates are of an order of magnitude of 1000 °C s $^{-1}$ (longitudinal) and 10 000 °C s $^{-1}$ (transverse), as was deduced from the pyrometer measurements. At these rates, the kinetics of γ' formation cannot be reasonably approximated by thermodynamic equilibrium.

The lack of other investigations of phase transformations in superalloys with comparable heating and cooling rates makes it difficult to classify the results based on the available literature. In particular, quantitative data of the γ' phase transformation at rates of temperature change encountered in AM is not yet available. Cooling with 100 K s $^{-1}$ yields small, irregular γ' precipitates, whereas slower cooling produces larger particles and may lead to nucleation bursts, creating multiple generations

www.aem-journal.com

of precipitates. $^{[41,42]}$ In this range of cooling rates, the formation of the γ' phase cannot be suppressed. $^{[43]}$ In general, the phase transformation rate was found to increase with accelerated cooling. $^{[44]}$ When heating a sample, it was found that the γ' phase under dissolution was further from equilibrium than under precipitation. $^{[41]}$ Our results align with these findings, as an extrapolation of the available data suggests that the γ' phase formation should be suppressed at sufficiently high cooling rates. We could thereby contribute to the understanding of the AM process by providing qualitative insight into the phase transformations under realistic process conditions.

5. Conclusions

We investigated the γ/γ' phase transformations during SLM of the nickel-base superalloy CMSX-4 using combined in situ SAXS and WAXS. Due to the short exposure times and a low fraction of γ' phase, a qualitative SAXS analysis was most appropriate. The integrated intensity Q' allowed us to obtain several insights into the dynamics of phase transformations induced by the characteristic heating and cooling cycles of an AM process:

- 1) Due to high cooling rates in the AM process as well as powder production, formation of the γ' phase is suppressed during solidification. In the powder and in the as-solidified state, only the supersaturated γ phase is present.
- 2) Small amounts of γ' phase form later in already solidified layers, induced by reheating when the overlying layers are molten. Some γ' phase may also form within the powder before melting.
- 3) Phase transformations take place at significantly off-equilibrium conditions. This enables the dissolution of the γ' phase at temperatures well below the equilibrium solvus temperature. During heating, both formation and dissolution of γ' take place.
- 4) The scanning strategy had a more decisive influence on the phase transformation dynamics than beam power or scanning speed. Further knowledge about the dependence of these non-equilibrium transformations on the thermal history could enable tailoring the precipitate microstructure by proper control of the process parameters.

Acknowledgements

The authors acknowledge DESY (Hamburg, Germany), a member of the Helmholtz Association HGF, for providing experimental facilities. Parts of this research were carried out at PETRA III. The authors thank Ulrich Lienert for his assistance in operating the beamline P21.2. The authors also thankfully acknowledge the German Research Foundation (DFG) and the Collaborative Research Center 103 Project C7 for carrying out the Thermo-Calc calculations as well as the Collaborative Research Center 814 Project B2 for performing the thermal simulations. Finally, the authors thank Florian Galgon, Tobias Gaag, and Daniel Gage for their support in conducting the in situ measurements at DESY.

Open access funding enabled and organized by Projekt DEAL.

Conflict of Interest

The authors declare no conflict of interest.

Data Availability Statement

The data that support the findings of this study are available from the corresponding author upon reasonable request.

Keywords

additive manufacturing, in situ measurements, phase transformations, X-ray scattering

Received: January 28, 2021 Revised: April 21, 2021 Published online: May 3, 2021

- [1] W. Kan, B. Chen, C. Jin, H. Peng, Mater. Des. 2018, 160, 611.
- [2] M. Ramsperger, C. Körner, in Superalloys 2016, Proc. Int. Symp. Superalloys, 13th (Eds: M. Hardy, E. Huron, U. Glatzel, B. Griffin, B. Lewis, C. Rae, V. Seetharaman, S. Tim), TMS, Seven Springs, PA 2016.
- [3] M. R. Gotterbarm, A.M. Rausch, C. Körner, Metals 2020, 10, 313.
- [4] J. A. Köpf, D. Soldner, M. Ramsperger, J. Mergheim, M. Markl, C. Körner, Comput. Mater. Sci. 2019, 162, 148.
- [5] L. Adler, Z. Fu, C. Körner, Mater. Sci. Eng. A 2020, 785, 139369.
- [6] C. Körner, Int. Mater. Rev. 2016, 61, 361.
- [7] A. A. Martin, N. P. Calta, S. A. Khairallah, J. Wang, P. J. Depond, A. Y. Fong, V. Thampy, G M. Guss, A. M. Kiss, K. H. Stone, C. J. Tassone, J. N. Weker, M. F. Toney, T. van Buuren, M. J. Matthews, Nat. Commun. 2019, 10, 1987.
- [8] C. A. L. Leung, S. Marussi, R. C. Atwood, M. Towrie, P. J. Withers, P. D. Lee, *Nat. Commun.* 2018, 9, 1355.
- [9] C. Zhao, K. Fezzaa, R. W. Cunningham, H. Wen, F. De Carlo, L. Chen, A. D. Rollett, T. Sun, Sci. Rep. 2017, 7, 3602.
- [10] J. Epp, J. Dong, H. Meyer, A. Bohlen, Scr. Mater. 2020, 177, 27.
- [11] C. Kenel, D. Grolimund, X. Li, E. Panepucci, V. A. Samson, D. Ferreira Sanchez, F. Marone, C. Leinenbach, Sci. Rep. 2017, 7, 16358.
- [12] S. Hocine, H. Van Swygenhoven, S. Van Petegem, C. S. T. Chang, T. Maimaitiyili, G. Tinti, D. Ferreira Sanchez, D. Grolimund, N. Casati, *Mater. Today (Oxford, U. K.)* 2020, 34, 30.
- [13] E. Chauvet, C. Tassin, J-J. Blandin, R. Dendievel, G. Martin, Scr. Mater. 2018, 152, 15.
- [14] C. Körner, M. Ramsperger, C. Meid, D. Bürger, P. Wollgramm, M. Bartsch, G. Eggeler, Metall. Mater. Trans. A 2018, 49, 3781.
- [15] P. Kontis, E. Chauvet, Z. Peng, J. He, A. K. da Silva, D. Raabe, C. Tassin, J-J. Blandin, S. Abed, R. Dendievel, B. Gault, G. Martin, Acta Mater. 2019, 177, 209.
- [16] Y. Li, K. Chen, N. Tamura, Mater. Des. 2018, 150, 171.
- [17] M. Ramsperger, R. F. Singer, C. Körner, *Metall. Mater. Trans. A* 2016, 47, 1496.
- [18] Y. T. Tang, J. N. Ghoussoub, C. Panwisawas, D. M. Collins, S. Amirkhanlou, J. W. G. Clark, A. A. N. Németh, D. G. McCartney, R. C. Reed, in *Superalloys 2020, Proc. Int. Symp. Superalloys, 14th* (Eds: S. Tin, M. Hardy, J. Clews, J. Cormier, Q. Feng, J. Marcin, C. O'Brien, A. Suzuki), TMS, Seven Springs, PA 2020.
- [19] I. Lopez-Galilea, B. Ruttert, J. He, T. Hammerschmidt, R. Drautz, B. Gault, W. Theisen, Addit. Manuf. 2019, 30, 100874.
- [20] V. D. Divya, R. Muñoz-Moreno, O. M. D. M Messé, J. S. Barnard, S. Baker, T. Illston, H. J. Stone, *Mater. Charact.* 2016, 114, 62.
- [21] B. Wahlmann, F. Galgon, A. Stark, S. Gayer, N. Schell, P. Staron, C. Körner, Acta Mater. 2019, 180, 84.



www.advancedsciencenews.com www.aem-journal.com

ENGINEERING MATERIALS

- [22] F. Schmeiser, E. Krohmer, N. Schell, E. Uhlmann, W. Reimers, Addit. Manuf. 2020, 32, 101028.
- [23] E. Uhlmann, E. Krohmer, F. Schmeiser, N. Schell, W. Reimers, Rev. Sci. Instrum. 2020, 91, 075104.
- [24] N. Schell, A. King, F. Beckmann, T. Fischer, M. Müller, A. Schreyer, Mater. Sci. Forum 2014, 772, 57.
- [25] P. Staron, T. Fischer, T. Lippmann, A. Stark, S. Daneshpour, D. Schnubel, E. Uhlmann, R. Gerstenberger, B. Camin, W. Reimers, E. Eidenberger, H. Clemens, N. Huber, A. Schreyer, Adv. Eng. Mater. 2011, 13, 658.
- [26] G. Benecke, W. Wagermaier, C. Li, M. Schwartzkopf, G. Flucke, R. Hoerth, I. Zizak, M. Burghammer, E. Metwalli, P. Müller-Buschbaum, M. Trebbin, S. Förster, O. Paris, S. V. Roth, P. Fratzl, J. Appl. Crystallogr. 2014, 47, 1797.
- [27] F. De Geuser, A. Deschamps, C. R. Phys. 2012, 13, 246.
- [28] D. M. Collins, N. D'Souza, C. Panwisawas, C. Papadaki, G. D. West, A. Kostka, P. Kontis, Acta Mater. 2020, 200, 959.
- [29] N. T. Nguyen, A. Ohta, K. Matsuoka, N. Szuuki, Y. Maeda, Weld. J. (Miami, FL, U. S.) 1999, 78, 265.
- [30] D. Rosenthal, Weld. J. (Miami, FL, U. S.) 1941, 20, 220.
- [31] B. Stump, A. Plotkowski, Appl. Math. Model. 2019, 75, 787.
- [32] Z. Zhang, Y. Huang, A. R. Kasinathan, S. I. Shahabad, U. Ali, Y. Mahmoodkhani, E. Toyserkani, Opt. Laser Technol. 2019, 109, 297.

- [33] A. Plotkowski, M. M. Kirka, S. S. Babu, Addit. Manuf. 2017, 18, 256.
- [34] B. Cheng, J. Lydon, K. Cooper, V. Cole, P. Northrop, K. Chou, J. Manuf. Process. 2018, 32, 744.
- [35] P. Strunz, D. Mukherji, R. Gilles, A. Wiedenmann, J. Rösler, H. Fuess, J. Appl. Crystallogr. 2001, 34, 541.
- [36] X. Wu, S. Lan, X. Wei, J. Zhou, Z. Lu, J. D. Almer, X-L. Wang, Appl. Phys. Lett. 2019, 114, 211903.
- [37] X. Liu, H. Li, M. Zhan, Manuf. Rev. 2018, 5, 10.
- [38] M. Hillert, Acta Mater. 1999, 18, 4481.
- [39] S. Meher, M. C. Carroll, T. M. Pollock, L. J. Carroll, *Mater. Des.* 2015, 140, 249.
- [40] J. O. Andersson, T. Helander, L. Höglund, P. F. Shi, B. Sundman, CALPHAD: Comput. Coupling Phase Diagrams Thermochem. 2002, 26. 273.
- [41] T. Grosdidier, A. Hazotte, A. Simon, Mater. Sci. Eng. A 1998, 256, 183.
- [42] A. R. P. Singh, S. Nag, S. Chattopadhyay, Y. Ren, J. Tiley, G. B. Viswanathan, H. L Fraser, R. Banerjee, Acta Mater. 2013, 61, 280.
- [43] S. S. Babu, M. K. Miller, J. M. Vitek, S. A. David, Acta Mater. 2001, 49, 4149.
- [44] F. Masoumi, D. Shahriari, J. Cormier, A. Devaux, Sci. Rep. 2016, 6. 28650.